PNAS RESEARCH ARTICLE | CHEMISTRY
BIOPHYSICS AND COMPUTATIONAL BIOLOGY OPEN ACCESS

Unveiling the catalytic mechanism of GTP hydrolysis in microtubules

Daniel Beckett[a] and Gregory A. Voth[a,1]

Edited by William Jorgensen, Yale University, New Haven, CT; received April 12, 2023; accepted May 16, 2023

Microtubules (MTs) are large cytoskeletal polymers, composed of αβ-tubulin heterodimers, capable of stochastically converting from polymerizing to depolymerizing states and vice versa. Depolymerization is coupled with hydrolysis of guanosine triphosphate (GTP) within β-tubulin. Hydrolysis is favored in the MT lattice compared to a free heterodimer with an experimentally observed rate increase of 500- to 700-fold, corresponding to an energetic barrier lowering of 3.8 to 4.0 kcal/mol. Mutagenesis studies have implicated α-tubulin residues, α:E254 and α:D251, as catalytic residues completing the β-tubulin active site of the lower heterodimer in the MT lattice. The mechanism for GTP hydrolysis in the free heterodimer, however, is not understood. Additionally, there has been debate concerning whether the GTP-state lattice is expanded or compacted relative to the GDP state and whether a "compacted" GDP-state lattice is required for hydrolysis. In this work, extensive quantum mechanics/molecular mechanics simulations with transition-tempered metadynamics free-energy sampling of compacted and expanded interdimer complexes, as well as a free heterodimer, have been carried out to provide clear insight into the GTP hydrolysis mechanism. α:E254 was found to be the catalytic residue in a compacted lattice, while in the expanded lattice, disruption of a key salt bridge interaction renders α:E254 less effective. The simulations reveal a barrier decrease of 3.8 ± 0.5 kcal/mol for the compacted lattice compared to a free heterodimer, in good agreement with experimental kinetic measurements. Additionally, the expanded lattice barrier was found to be 6.3 ± 0.5 kcal/mol higher than compacted, demonstrating that GTP hydrolysis is variable with lattice state and slower at the MT tip.

GTP hydrolysis | microtubule | free energy | QM/MM | multiscale

Significance

Microtubules (MTs) are large and dynamic components of the eukaryotic cytoskeleton with the ability to stochastically convert from a polymerizing to a depolymerizing state and vice versa. Depolymerization is coupled to the hydrolysis of guanosine-5′-triphosphate (GTP), which is orders of magnitude faster in the MT lattice than in free tubulin heterodimers. Our results computationally ascertain the catalytic residue contacts in the MT lattice that accelerate GTP hydrolysis compared to the free heterodimer as well as confirm that a compacted MT lattice is necessary for hydrolysis, while a more expanded lattice is unable to form the necessary contacts and thereby hydrolyze GTP.

Microtubules (MTs) are ubiquitous components of the eukaryotic cytoskeleton that play key roles in a plethora of cellular processes, including serving as tracks for motor proteins and creation of the dynamic mitotic spindle during mitosis (1–3). A specific property of MTs that allows them to fulfill such diverse roles is dynamic instability (DI), wherein growing MTs stochastically switch from a polymerizing state to a depolymerizing state (MT catastrophe) and vice versa (rescue) (4–6). The delicate balance of the DI process makes the MT a potent drug target to treat multiple cancers through the manipulation of MT structure and catalytic activity, in order to either discourage or encourage depolymerization (7–10).

MTs are assembled from tubulin heterodimers, each composed of an α- and β-tubulin monomer, which stack into protofilaments (PFs) and laterally associate into tubules. Both monomeric tubulin subunits bind a molecule of guanosine triphosphate (GTP), in the free heterodimer, β-tubulin sits atop the GTP binding site of α-tubulin, while in the microtubule lattice, the α-tubulin of one heterodimer sits atop the GTP binding site of another heterodimer's β-tubulin (Fig. 1 *A*–*C*). GTP bound by α-tubulin is not hydrolyzed or exchanged in solution with other GTP molecules, whereas GTP bound by β-tubulin can hydrolyze to guanosine diphosphate (GDP), and subsequently, GDP can be exchanged at the microtubule tip, or in the free heterodimer, for GTP. These observations have led to the α-tubulin GTP-binding site to be called the nonexchangeable site (N-site), while β-tubulin possesses the exchangeable site (E-site) (11–14). While it is known that the hydrolysis of GTP at the E-site is coupled to microtubule depolymerization and catastrophe, the exact mechanism behind this is not fully understood, and insights into the actual hydrolysis mechanism would be invaluable (15, 16).

GTP hydrolysis has been known to be faster in the MT lattice than the free heterodimer, with recent experiments anticipating a rate difference of 500- to 700-fold, corresponding to an energetic barrier difference of 3.9 ± 0.1 kcal/mol (17, 18). Cryo-EM measurements and mutagenesis studies have led to the hypothesis that specific α-tubulin residues (α:E254 and α:D251) complete the β-tubulin GTPase site and catalyze hydrolysis (18–22). Additionally, when a nonhydrolyzable GTP-mimic, GMPCPP, is used in place of GTP, the MT lattice seems to be expanded relative to the GDP lattice, which supports the hypothesis

Author affiliations: [a]Department of Chemistry, Chicago Center for Theoretical Chemistry, Institute for Biophysical Dynamics, and James Franck Institute, The University of Chicago, Chicago, IL 60637

Author contributions: D.B. and G.A.V. designed research; D.B. performed research; D.B. analyzed data; and D.B. and G.A.V. wrote the paper.

The authors declare no competing interest.

This article is a PNAS Direct Submission.

[1]To whom correspondence may be addressed. Email: gavoth@uchicago.edu.

This article contains supporting information online at https://www.pnas.org/lookup/suppl/doi:10.1073/pnas.2305899120/-/DCSupplemental.

Published June 26, 2023.

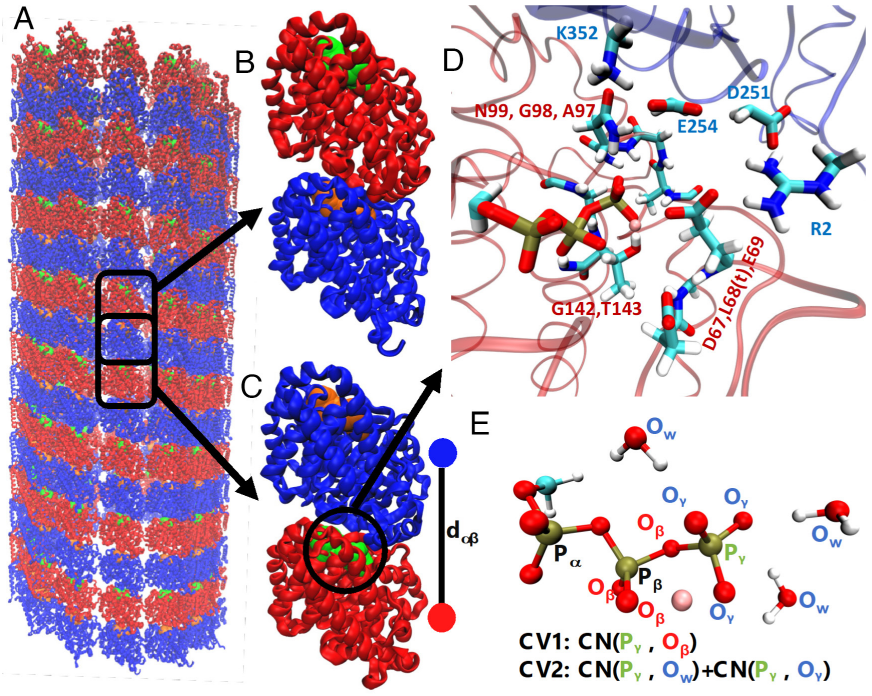

Fig. 1. Schematics of systems studied: (*A*) cartoon of a full microtubule, plus-end on top, with β-tubulin in red, α-tubulin in blue, GTP bound by β-tubulin in green, and GTP bound by α-tubulin in orange; (*B*) example of a tubulin αβ-heterodimer; (*C*) example of an interdimer complex formed by the α-tubulin of one heterodimer sitting above the β-tubulin of another, with $d_{\alpha\beta}$ defined as the distance between the centers of mass of the monomers; (*D*) the QM region used in this study for interdimer complexes (more description in *Materials and Methods*), with magnesium in pink, (*E*) labeled atoms for reaction coordinate definitions as seen in Fig. 2: the *X* axis is the coordination number of P_γ to O_β; the *Y* axis is the coordination number of P_γ to O_γ plus the coordination number of P_γ to O_w.

that lattice compaction induced by hydrolysis incurs strain on the MT lattice, which in turn is released by catastrophe (23, 24). Recent work using inorganic phosphate mimics has implied that expansion is an artifact of GMPCPP in the lattice, which would also imply that lattice compaction is necessary for hydrolysis rather than a result of it (25). Finally, recent cryo-EM analysis of mutated (α: E254A/N) MT has revealed that the expanded GMPCPP state may more closely resemble tubulin at the MT tip (26).

The present study aims to deconvolute the discussion of microtubule structure by investigating GTP hydrolysis both in an expanded and compacted MT lattice as well as in the free heterodimer. Through the use of transition-tempered metadynamics (TTMetaD) enhanced free-energy sampling combined with quantum mechanics/molecular mechanics (QM/MM) simulation, we have mapped the free-energy surface of GTP hydrolysis and affirmed the importance of the α:E254 residue in the catalytic activity of the compacted lattice. We have determined that the activation barrier of hydrolysis in the free heterodimer is 3.8 ± 0.5 kcal/mol higher than in the compacted lattice, in good agreement with the experimental value of 3.9 ± 0.1 kcal/mol. Furthermore, hydrolysis in the expanded lattice was found to have a higher barrier than even the free heterodimer, potentially due to disruption of a critical intersubunit salt bridge interaction making α:E254 unreachable. These explicit simulation results confirm the catalytic role of the α:E254 residue while also demonstrating that lattice compaction is essential for facile GTP hydrolysis.

Results and Discussion

A Compacted Interdimer MT Lattice Hydrolyzes GTP More Readily Than an Expanded Lattice or Free Heterodimer. GTP hydrolysis was explored in 3 systems as illustrated in Fig. 1 *A*–*C*: a free tubulin heterodimer, an interdimer complex restrained at a "compacted" GDP-like interdimer distance ($d_{\alpha\beta}$ = 40.5 Å), and an "expanded" interdimer complex held at an interdimer distance close to that observed in the tip of an MT ($d_{\alpha\beta}$ = 42.0 Å). In all cases, 10 replicas were employed for QM/MM TTMetaD along two collective variables (CVs) to define hydrolysis. The final two-dimensional free energy surfaces for GTP hydrolysis in each system can be seen in Fig. 2. The QM region and employed CVs can be seen in Fig. 1 *D* and *E*, respectively, with additional details presented in the *Materials and Methods*.

In Fig. 2, the *X* axis represents the coordination number of the leaving dissociating phosphate phosphorus atom to the GDP end phosphate oxygens and varies from ~1 in the reactant well to ~0 in the product well. The *Y* axis shows the coordination number of the phosphorus atom to its own phosphate oxygens as well as any water oxygens and varies from ~3 in the reactant well to ~4 in the product well. A "fully associative" path from reactant to product would be a near-vertical line from the reactant well followed by a near-horizontal line to the products, whereas a "fully dissociative" path would be a nearly horizontal line from the reactant well followed by a nearly vertical line to products. A diagonal line from the reactant to the product would be a more concerted path wherein dissociation from GDP is coupled to association of water, similar to that observed in ATP hydrolysis in actin and likely accelerated by a catalytic residue (27, 28). In the case of the compacted interdimer complex, a concerted path was found to be the lowest free-energy pathway connecting reactants to products, while in the expanded interdimer complex and the free heterodimer, a more dissociative pathway was preferred. In both the free heterodimer and the expanded interdimer complex, a concerted mechanism was also found but higher in free energy than the dissociative route. Discussion of other possible pathways can be found in *SI Appendix*.

The energetics along the minimum free-energy paths (MFEPs) are shown in Fig. 2*D* with progress along the pathway interpolated from 0 (reactant well) to 1 (product well). It is clear from Fig. 2*D* that the lowest energy transition state for any system is along the

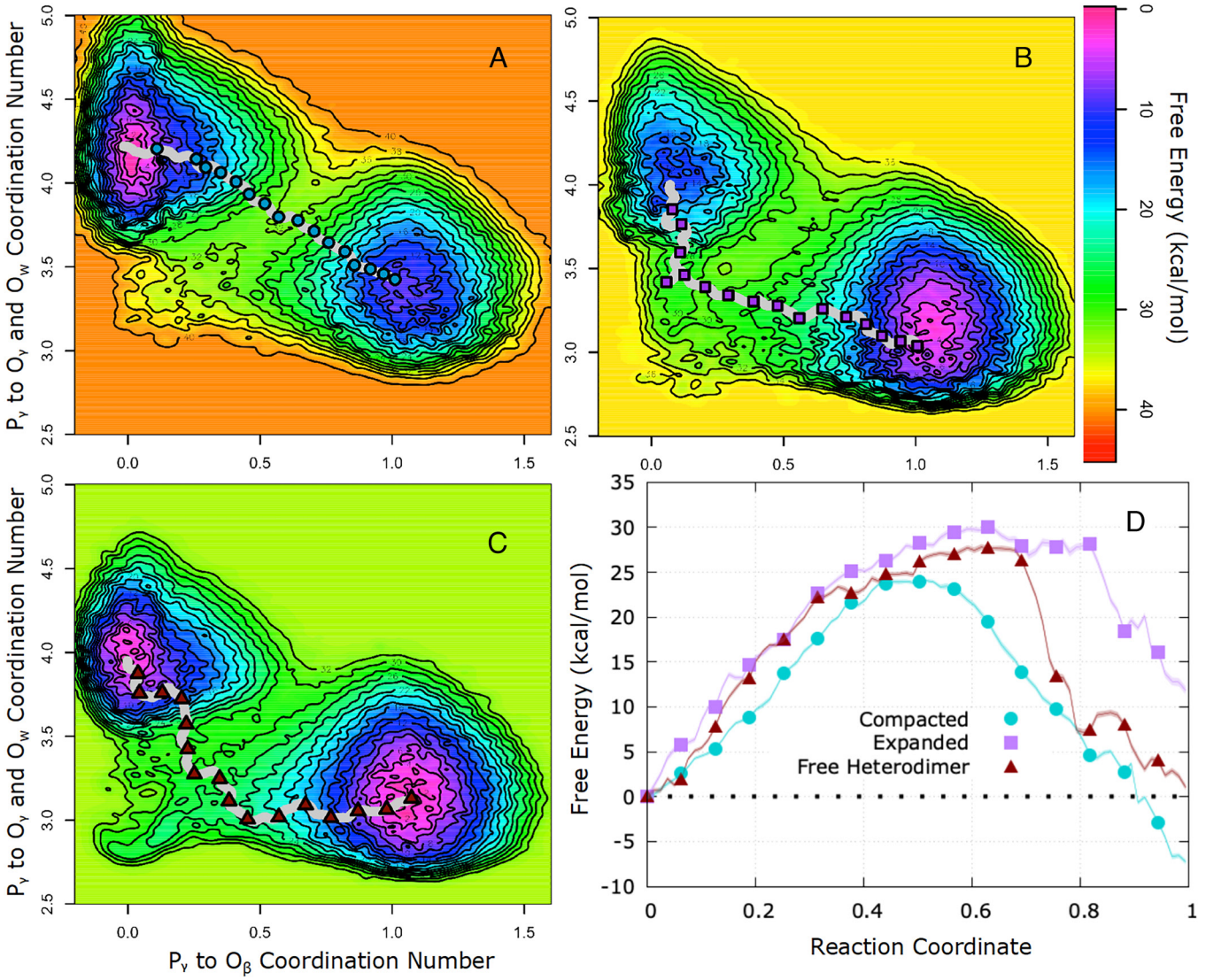

Fig. 2. Final converged free-energy surfaces for GTP hydrolysis in each system with the lowest-energy pathway shown as a gray line with symbols overtop: (*A*) compacted interdimer complex, (*B*) expanded interdimer complex, (*C*) free heterodimer, and (*D*) the free energy along the lowest-energy pathway in each system with error shown as the transparent shading around each line. Topological lines in *A*–*C* drawn every 2 kcal/mol. Each pathway is represented by 160 points in total; every 10th point is represented as a visible point on the plot for comparison. The *X* axis in 2D scales progress along the reaction path from 0 (reactant well) to 1 (product well).

concerted pathway in the compacted interdimer complex, at 24.0 ± 0.2 kcal/mol. As was the case in actin, the barriers are somewhat higher than that expected from experimental rates given the known error in the electronic density functional (DFT) utilized in the QM/MM, but we are primarily interested in the differences between the pathways as that error then cancels out (27, 28). The barrier for the free heterodimer MFEP is 3.8 ± 0.5 kcal/mol higher than compacted, while the barrier for the expanded interdimer complex is 6.3 ± 0.5 kcal/mol higher than compacted. The rate difference between the compacted and free heterodimer–concerted pathways corresponds well to recent experimental measurements of GTP hydrolysis in an MT ($0.16\ s^{-1}$) versus free tubulin ($0.0003\ s^{-1}$), which translates to an energetic difference of 3.9 kcal/mol (17). Another recent study comparing wild-type MTs to E254D mutants determined a rate of $0.2\ s^{-1}$ for GTP hydrolysis in an MT, corresponding to an energy difference with the free tubulin measurement of 4.00 kcal/mol (18). Comparing these experimental values gives us a kinetic barrier of 3.9 ± 0.1 kcal/mol, which is in excellent agreement with our compacted vs. free heterodimer concerted pathway barrier difference of 3.8 ± 0.5 kcal/mol. This agreement, as well as the high barrier for hydrolysis in the expanded interdimer complex, confirms that lattice compaction is necessary for GTP hydrolysis in an MT.

αE254 Is the Catalytic Residue in the Compacted Lattice, but Unreachable in Expanded. Full movies displaying each type of reaction (concerted and dissociative) for each system can be seen in *SI Appendix* along with the replica ID of the TTMetaD trajectory from which it was taken. Complete 2 CV trajectories overlayed over the free-energy surfaces shown in Fig. 2 for each replica in each system can also be found in *SI Appendix*.

Fig. 3 shows representative snapshots for the minimum free-energy pathway in each system, taken directly from the appropriate trajectory. The first panel of each row shows the initial proton transfer from the lytic water. In the compacted interdimer complex (Fig. 3*A*), α:E254 serves as the catalytic residue and initiates the deprotonation. This is in line with mutagenesis experiments in both human tubulin and yeast that found an α:E254A mutation to prohibit GTP hydrolysis (18, 21). In every observed crossing in the compacted interdimer complex, α:E254 always

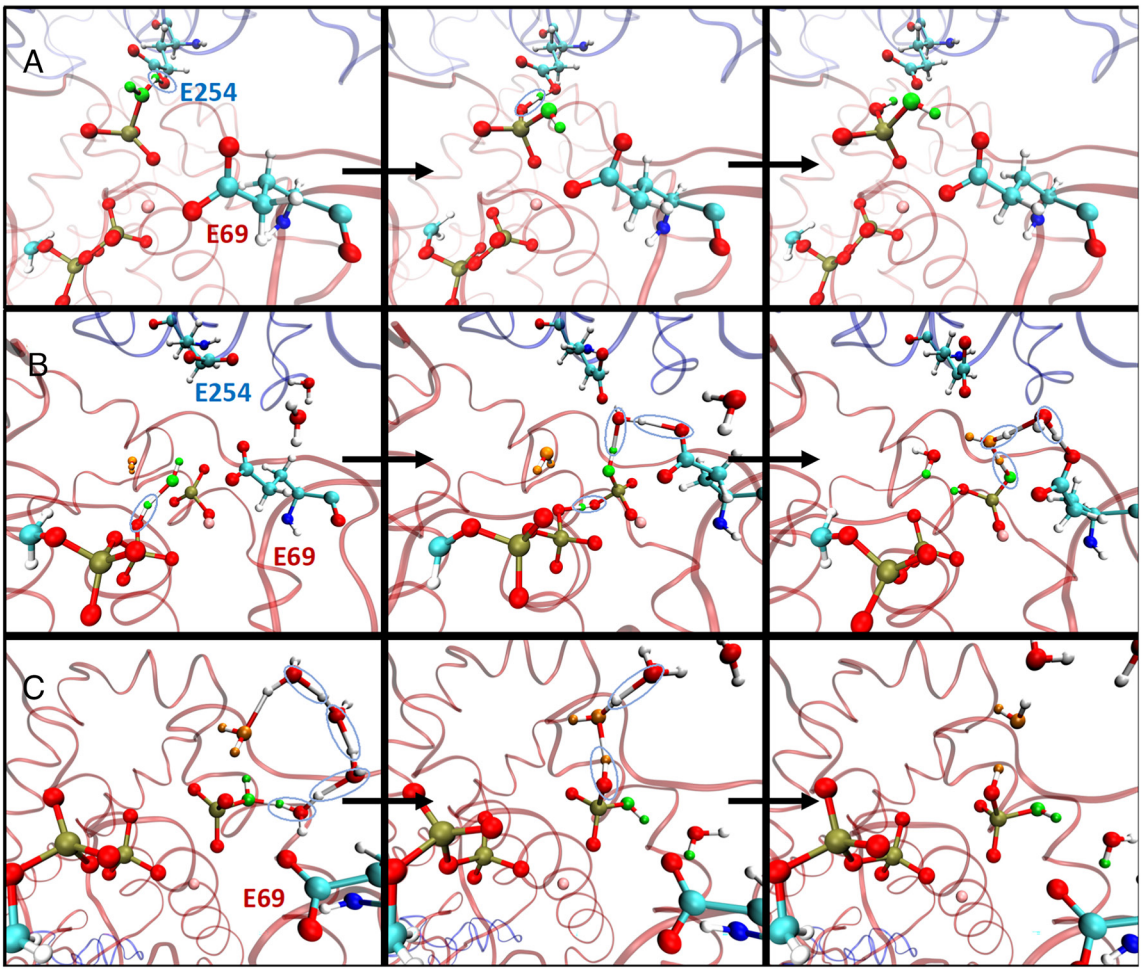

Fig. 3. Snapshots of proton rearrangements from metadynamics trajectories for lowest-energy reaction pathways in (*A*) compacted interdimer complex (taken from replica ID "W0") (*B*) expanded interdimer complex (W0), and (*C*) free heterodimer (W0). Lytic water associating with leaving phosphate is colored green, additional water depositing proton onto the phosphate is colored orange when present (*B* and *C*), and magnesium is shown in pink. Bonds are drawn with a 1.8-Å cutoff: Only critical residues are shown atomically (labeled on the first slide), and red ribbons represent β-tubulin while blue ones represent α-tubulin. The first column shows initial proton transfer, the second column is proton transfer to form H_2PO_4, and the third column shows final product after formation (*A* and *C*) or final proton transfer (*B*). Blue translucent ovals highlight proton transfers: Circled atoms generally remain bonded after the given frame, though in *C*, this is difficult to define due to the long chain of proton transfers in panels 1 and 2, which occur in quick succession. Movies pulled directly from the appropriate trajectory for each mechanism shown here can be found in *SI Appendix*.

fills this role and always does so directly without a water wire being necessary. After the initial deprotonation, the proton is deposited onto an O_γ (Fig. 3*A*, panel 2) to form the final H_2PO_4 product (Fig. 3*A*, panel 3).

In the free heterodimer (Fig. 3*C*), where the α-tubulin residues are unavailable, PO_3^- dissociates far enough from the GDP to form a water wire with itself that deprotonates the associated H_2O (Fig. 3*C*, panel 1) and protonates another O_γ (panel 2) to form H_2PO_4. This mechanism results from the trajectory that most closely matches the MFEP shown in Fig. 2*C*; however, other higher-energy dissociative crossings, similar to the expanded interdimer complex, were observed. In the expanded lattice (Fig. 3*B*), the presence of the α-tubulin prevents the water wire mechanism seen in the free heterodimer, and instead, a β phosphate oxygen serves to initiate deprotonation as the lytic water inserts between the β and γ phosphates. In the subsequent panel, β:E69 coordinates the hydroxyl group via a second water and abstracts the second proton, while the original proton on the O_β is deposited onto a second O_γ. In the third panel, a final proton transfer is shown, where the proton from the orange water is deposited onto the lytic water oxygen through another water wire interaction with β:E69. A second, more direct, mechanism was seen in the expanded interdimer complex that would follow the same MFEP, wherein the lytic water was simultaneously coordinated by O_β and β:E69 before deprotonation by O_β. Additionally, concerted pathways involving deprotonation of the lytic water by β:E69 were seen in both the free heterodimer and expanded interdimer complex. These pathways are slightly higher in energy (<1 kcal/mol) than the dissociative pathways and worth consideration as possible mechanisms in the less favorable systems. All alternate mechanisms and free-energy paths are documented in *SI Appendix*.

Interestingly, there were no observed TTMetaD barrier crossings in the expanded interdimer complex that resulted from deprotonation by α:E254. Occasionally, α:E254 is close enough to the lytic water to loosely coordinate a hydrogen (as can be seen in Fig. 3*B*, panel 2), but it does not directly participate in hydrolysis. To understand why α:E254 is unable to serve as the catalytic residue in the expanded interdimer complex, Fig. 4 compares geometric parameters within the E-site between the compacted and expanded conformations. Most immediately observable is the change in the angle formed by the phosphorus atoms (P_α–P_β–P_γ) in the GTP chain, illustrated by the green line in Fig. 4*A*. This difference in the phosphate chain angle is quantified in Fig. 4*G*, comparing the normalized probability

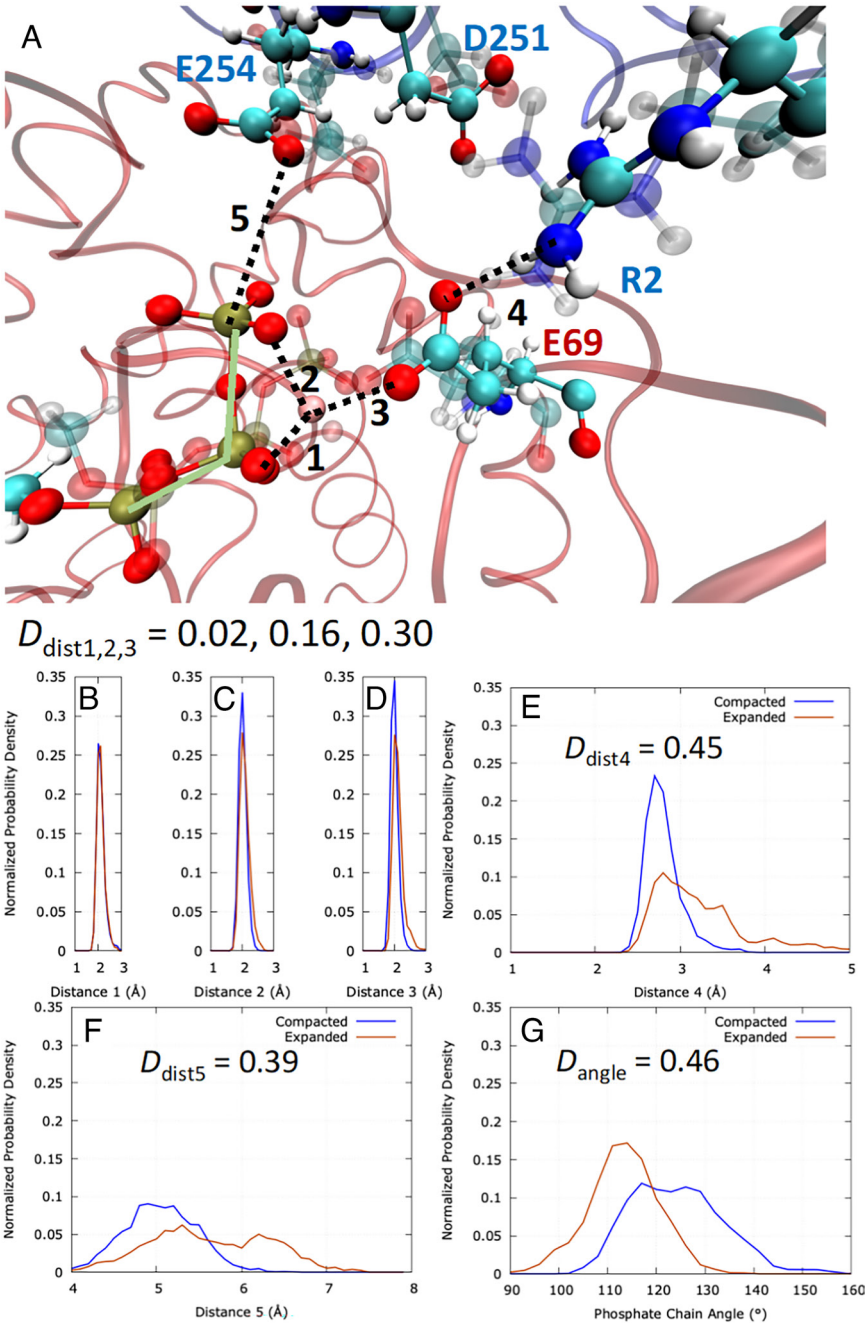

Fig. 4. Comparisons of expanded vs. compacted interdimer complex geometric parameters within the E-site. (*A*) CPK rendering of compacted (solid) and expanded (transparent) residues with the compacted protein environment shown as transparent ribbons, taken from the first frame of metadynamics simulation. (*B–F*) Normalized probability distributions of the distances labeled in *A*, computed over the 50-ps reaction well "seed trajectories." (*G*) Normalized probability distribution of the phosphate chain angle (P_α-P_β-P_γ) over the seed trajectories, illustrated as a green line in *A*. Kolmogorov–Smirnov statistic (*D*) between the expanded and compacted distributions shown for each plot. Labeled distances: **1** nearest O_β to Mg, **2** nearest O_γ to Mg, **3** nearest β:E69 carboxylate O to Mg, **4** nearest β:E69 carboxylate O to α:R2 guanidinium N, **5** P_γ to nearest α:E254 carboxylate O.

distribution over the initial 50-ps metadynamics seed trajectories (a diagram of these trajectories and all trajectories are available in *SI Appendix*); the compacted phosphate chain is able to sample a range of more obtuse angles, putting it in line with the α:E254 carboxylate group.

To quantify the difference between the normalized probability distributions of the compacted complex and the expanded complex, we employ the Kolmogorov–Smirnov statistic, *D*, a measure of distance between two probability distributions which is defined as the maximum absolute difference in the cumulative distribution functions (29, 30). A value of 0 would correspond to identical distributions, while a value of 1 (when applied to normalized distributions) would correspond to distributions with no overlap whatsoever. A total of five critical contacts are labeled in Fig. 4*A*: The two involving the negatively charged β and γ phosphate oxygen atoms and the Mg^{2+} ion (Fig. 4 *B* and *C*) have the lowest KS statistics. In both complexes, the β:E69 residue coordinates Mg^{2+}, and the expanded complex experiences slightly higher lengths of this interaction (Fig. 4*D*); however, it is the interdimer interaction of α:R2 and β:E69 (between the positively charged guanidinium N and the negatively charged carboxylic acid O) that displays the highest KS statistic (Fig. 4*E*). While this distance in the compacted complex peaks strongly at 2.7 Å, in the expanded complex, the α:R2 to β:E69 distance meanders and cannot form steadily. In the

compacted complex, the low distance between the R and E heavy atoms qualifies as a complex salt bridge interaction, but the interaction is degraded in the expanded complex (31, 32). Degradation of the α:R2–β:E69 interaction is more pronounced than any other in the immediate E-site binding pocket and likely corresponds to the dip in the phosphate chain angle (Fig. 4*G*) and the increase in the critical α:E254–P_γ distance (Fig. 4*F*) that allows α:E254 to function as a catalytic residue. Mutagenesis of α:R2 to either a complete deactivation (α:R2A) or damping the interaction (α:R2K) would be an interesting comparison in the future to determine whether this has an effect on the rate of hydrolysis in a growing MT.

Conclusions

GTP hydrolysis in a microtubule is coupled to the onset of depolymerization. The regulation of this reaction is essential to the operation of microtubule-associated proteins and drugs targeting their function. Structurally, the hydrolysis of GTP to GDP has been suggested to result in lattice compaction with the nonhydrolyzable GMPCPP mimic and the microtubule tip structure displaying an expanded lattice. Furthermore, the E254 and E251 residues of the α tubulin belonging to the heterodimer above a given β-tubulin-bound GTP have been implicated by mutagenesis experiments as critical to hydrolysis (18, 21). Extensive QM/MM TTMetaD simulations on a compacted interdimer tubulin complex, an expanded interdimer tubulin complex, and a free tubulin heterodimer have been reported in this work in order to untangle the effects of compaction and confirm the identity of certain catalytic residues.

Ten TTMetaD QM/MM replicas were run for each system, for a total of ~10 M cpu*hours of simulation time. In the compacted interdimer complex, a concerted pathway is strongly favored, and α:E254 directly participates in hydrolysis. In the expanded interdimer complex, the triphosphate chain is unable to coordinate a water close enough to the α:E254 carboxylate for it to aid in hydrolysis. This effect may be a result of an interdimer salt bridge between α:R2 and β:E69 that is persistent in the compacted lattice but is not fully established in the expanded.

In both the free heterodimer and the expanded interdimer complex, a more dissociative pathway was found where the lytic water was deprotonated by the β phosphate oxygens either directly or through a water wire. In both the expanded lattice and the free heterodimer, the dissociative route was somewhat more favorable than a concerted route using the inconveniently located β:E69 residue. The lowest barrier difference between the free heterodimer and the compacted interdimer complex is 3.8 ± 0.5 kcal/mol, corresponding very well to the experimental value of 3.9 ± 0.1 kcal/mol. Last, the expanded interdimer complex barrier is 6.3 ± 0.5 kcal/mol higher than the compacted case, confirming that a compacted lattice is essential for facile GTP hydrolysis in a MT and that α:E254 serves as the catalytic factor in the compacted lattice. Furthermore, given the recent cryo-EM measurements of an expanded MT tip (33), these results imply that GTP hydrolysis proceeds very slowly in the tip compared to within the interior region of the MT.

Materials and Methods

System Setup and Equilibration. The initial structures for the free heterodimer and the interdimer complex were pulled from the 150-ns point on a previous full MT MD simulation of an 8-dimer long 13-PF MT (33). A single β-tubulin was chosen from the "back" PF of the MT (opposite to the seam) and the middle layer. For the interdimer complex, the α-tubulin about this β-tubulin was extracted, while for the free heterodimer, the α-tubulin below was extracted. This was done to ensure the same initial β-tubulin GTP-binding site configuration for each system. Each system was initially equilibrated in the NVT ensemble for 100 ns in a 121.5-Å side-length cubic periodic box (124.4 Å for the free heterodimer) with 100 mM NaCl at 310 K using the CHARMM36m force field and GROMACS 2019.4 (34, 35). The time step for equilibration was 2 fs, and smooth particle mesh Ewald electrostatics were used for the MM throughout both this step and the QM/MM to follow (36).

The free heterodimer was able to relax without restraints, while the interdimer complex was restrained at either the compacted or expanded C_α and C_β center-of-mass (CoM) distance between the α- and β-tubulin monomers with a harmonic force constant of 59.75 kcal/mol$Å^2$. The force constant was chosen that reproduced fluctuations in the interdimer distance most closely to those observed in the MT tip simulations (33). The compacted αβ CoM distance, 40.5 Å, was determined from the atomic model cryo-EM structure of an undecorated GDP lattice patch with accession code 6DPV (24). The expanded αβ CoM distance, 42.0 Å, was derived from the average over all interdimer distances in the "back" lattice patch of the full MT tip simulations (PFs 5 through 9 when counting from the seam and dimers 3 through 6) over the last 100 ns of the 200-ns total trajectories (33).

QM/MM Setup. Enhanced free-energy sampling of the GTP hydrolysis in each system was simulated using the QM/MM hybrid technique as implemented in CP2K version 6.1 with a 0.5-fs timestep (37–40). The MM environment was at the same level as described in the previous section. The QM level of theory used was the PBE density functional, with D3 dispersion corrections and zero damping, using the TZV2P basis set and GTH pseudopotential for the magnesium ion core electrons (41–46). All simulations were run in the NVT ensemble with a 121.5 Å side-length cubic periodic box (124.4 Å for the free heterodimer), 100 mM NaCl, and at 310 K using a Nosé–Hoover thermostat.

The quantum region for the interdimer complexes included the GTP truncated as a methyl triphosphate, the associated magnesium atom, waters within 6 Å of the γ-phosphate (7 Å for the free heterodimer), and eight β-tubulin and four α-tubulin amino acids near the phosphate tail. β-tubulin amino acids included in the QM region were Asp67, Leu68 (sidechain truncated), Glu69, Ala97, Gly98, Gln99, Gly142, and Thr143. For each contiguous chain of amino acids, the peptide bond was included in the QM region, and truncation occurred on the neighboring amino acid; for example, in the case of Asp67, the carbonyl group of Val66 was included. α-tubulin amino acids included were Arg2, Asp251, Glu254, and Lys352. Each α-tubulin residue was not in a contiguous chain and was represented only by the sidechain through severing after the last CH_2 group in the sidechain; for example, the bond between C_β and C_γ was cut in Glu254. Every cut bond was capped with a hydrogen atom. In the case of the free heterodimer, only the β-tubulin amino acids were included. Waters in the QM region were updated every 12 h of wall time, which ranges from 0.5 to 1 ps of simulation time. Overall, not including link atoms, the interdimer complex QM region consisted of 140 nonwater atoms with an average of 19 waters in the region at any given time for an average total of 197 QM atoms. The free heterodimer consisted of 109 nonwater atoms with an average of 27 QM waters for an average total of 190 QM atoms. The full system size for interdimer simulations was 182,697 atoms, while for the free heterodimer, the full size was 194,276 atoms, with 13,519 atoms being the actual dimer (protein, GTP, Mg).

Transition-Tempered Metadynamics Simulations. To enable the sampling of the GTP hydrolysis reaction, TTMetaD was employed. TTMetaD is a convergent form of metadynamics wherein Gaussian hills of changing height are dropped, with the hill height scaled by the smallest hill height deposited on the lowest barrier separating two basins (reactant and product) (47). Previous work testing convergent metadynamics on the hydrolysis of adenosine triphosphate (ATP) in actin found TTMetaD to outperform well-tempered metadynamics; however, recrossings from the product to reactant well were not observed (using any form of MetaD) (28). To increase the number of transitions observed in the present study, a multiple walker scheme was employed wherein multiple walkers add on to the same PMF (48). For each of the three systems studied, after an initial-50 ps seed metadynamics run, five pairs of walkers ran serially (pair 2 starting after pair 1 and so on) for 70 ps each for a total of 750 ps of simulation per system (and ~10 million cpu*hours used). Pairs of walkers were launched consecutively for 70 ps each until convergence (barrier energy error <0.5 kcal/mol, vide infra) was reached. Metadynamics parameters and a sample TTMetaD Plumed input section can be found in *SI Appendix*.

Two collective variables (CVs) were used to characterize GTP hydrolysis, similar to those used in previous studies of ATP hydrolysis in actin (27, 28). The dissociation of phosphate from GDP was captured via the coordination number between P_γ and O_β (Fig. 1*E* labels atoms involved in CVs); this CV is shown as the *X* axis in Fig. 2 and varies from roughly 1 in the reactant well to 0 in the product well. Coordination numbers were used instead of distances to allow ambiguity, such that P_γ could equally recombine with any O_β. The association of water with P_γ was captured by the coordination number of P_γ with O_w and P_γ with O_γ; this CV is shown as the *Y* axis in Fig. 2 and varies from roughly 3 in the reactant well to over 4 in the product well. Additional information on the modeling of coordination numbers can be found in *SI Appendix*.

All enhanced free-energy sampling was carried out using the open-source, community-developed PLUMED library (interfaced with CP2K), version 2.5.3 (49, 50). Free-energy surfaces were obtained and visualized (Fig. 2) with the Metadynminer R package (51). Minimum free-energy paths (MFEPs) were obtained through the Metadynminer package with the nudged elastic band (NEB) method linking intermediate wells (52). Concerted pathways were obtained by NEB directly from the reactants to the products, while the dissociative pathways were formed through concatenation of two NEBs, one linking reactants to a local minimum outside of the two basins and one linking the local minimum to the products. The number of points included in each NEB for the dissociative pathway is proportional to the CV distance of the line segment connecting the two basins, with a total of 160 points for every reported pathway. In all three systems, one walker engaged in a phosphorylation interaction wherein the dissociating PO_3^- interacts strongly with a glutamic acid residue for the remainder of the run. This was an artifact of sampling that could not lead to the product well without backtracking on the potential energy surface and was removed. This artifact and its removal are discussed in *SI Appendix*.

In order to estimate errors in the MFEPs, the collective variables for every replica were concatenated and reweighted using the final PMF; then, block analysis was done. Due to the irregular shape of the sampled region of the PMF in CV space, a full averaged error would be inappropriate, and instead, the average error on each individual point along the MFEP was obtained from blocks containing 40,000 to 50,000 timesteps. The goal for convergence for this work was to obtain an error on the barrier of less than 0.5 kcal/mol, which was obtained for all systems after 10 walkers had reached 70 ps each.

Data, Materials, and Software Availability. All simulation trajectories are available upon reasonable request to the authors.

ACKNOWLEDGMENTS. This research was supported by the National Institute of General Medical Sciences of the NIH through Fellowship F32 GM140646 (D.B.) and by the US Department of Energy, Office of Science, Basic Energy Sciences, under Award DE-SC0023318 (G.A.V.) (for latter-phase methods and analysis). Computational resources were provided by the University of Chicago Research Computing Center and the US Department of Defense High Performance Computing Modernization Program.

1. H. V. Goodson, E. M. Jonasson, Microtubules and microtubule-associated proteins. *Cold Spring Harb. Perspect. Biol.* **10**, a022608 (2018).
2. T. D. Pollard, R. D. Goldman, Overview of the cytoskeleton from an evolutionary perspective. *Cold Spring Harb. Perspect. Biol.* **10**, a030288 (2018).
3. H. Lee Sweeney, E. L. F. Holzbaur, Motor proteins. *Cold Spring Harb. Perspect. Biol.* **10**, a021931 (2018).
4. T. Mitchison, M. Kirschner, Dynamic instability of microtubule growth. *Nature* **312**, 237–242 (1984).
5. M. Coue, V. A. Lombillo, J. R. Lombillo, McIntosh, microtubule depolymerization promotes particle and chromosome movement *in vitro*. *J. Cell Biol.* **112**, 1165–1175 (1991).
6. M. K. Gardner, M. Zanic, J. Howard, Microtubule catastrophe and rescue. *Curr. Opin. Cell Biol.* **25**, 14–22 (2013).
7. E. Pasquier, M. Kavallaris, Microtubules: A dynamic target in cancer therapy. *IUBMB Life* **60**, 165–170 (2008).
8. E. Mukhtar, V. M. Adhami, H. Mukhta, Targeting microtubules by natural agents for cancer therapy. *Mol Cancer Ther.* **13**, 275–284 (2014).
9. R. A. Stanton, K. M. Gernert, J. H. Nettles, R. Aneja, Drugs that target dynamic microtubules: A new molecular perspective. *Medi. Res. Rev.* **31**, 443–481 (2011).
10. M. O. Steinmetz, A. E. Prota, Microtubule-targeting agents: Strategies to hijack the cytoskeleton. *Trends Cell Biol.* **28**, 776–792 (2018).
11. T. J. Mitchison, Localization of an exchangeable GTP BZinding site at the plus end of microtubules. *Science* **261**, 1044–1047 (1993).
12. M. Menéndez, G. Rivas, J. F. Diáz, J. M. Andreu, Control of the structural stability of the tubulin dimer by one high affinity bound magnesium ion at nucleotide N-site*. *J. Biol. Chem.* **273**, 167–176 (1998).
13. E. Nogales, Structural insights into microtubule function. *Annu. Rev. Biochem.* **69**, 277–302 (2000).
14. F.-A. Piedra *et al.*, GDP-to-GTP exchange on the microtubule end can contribute to the frequency of catastrophe. *Mol. Biol. Cell* **27**, 3515–3525 (2016).
15. D. Pantaloni, M. F. Carlier, R. Melki, C. Combeau, C. Valentin-Ranc, Role of nucleotide hydrolysis in the dynamics of actin filaments and microtubules. *AIP Conf. Proc.* **226**, 18–28 (1991).
16. H. P. Erickson, E. T. O'Brien, Microtubule dynamic instability and GTP hydrolysis. *Annu. Rev. Biophys. Biomol. Struct.* **21**, 145–166 (1992).
17. M. Paydar, B. H. Kwok, Evidence for conformational change-induced hydrolysis of β-tubulin-GTP. bioRxiv [Preprint] (2020). https://doi.org/10.1101/2020.09.08.288019 (Accessed 10 September 2020).
18. J. Roostalu *et al.*, The speed of GTP hydrolysis determines GTP cap size and controls microtubule stability. *eLife* **9**, e51992 (2020).
19. K. H. Downing, E. Nogales, Tubulin structure: Insights into microtubule properties and functions. *Curr. Opin. Struct. Biol.* **8**, 785–791 (1998).
20. E. Nogales, M. Whittaker, R. A. Milligan, K. H. Downing, High-resolution model of the microtubule. *Cell* **96**, 79–88 (1999).
21. K. R. Anders, D. Botstein, Dominant-lethal α-tubulin mutants defective in microtubule depolymerization in yeast. *Mol. Biol. Cell* **12**, 3973–3986 (2001).
22. J. LöweH. LiK. H. DowningE. Nogales, Refined structure of αβ-tubulin at 3.5 Å resolution. *J. Mol. Biol.* **313**, 1045–1057 (2001).
23. G. M. Alushin *et al.*, High-resolution microtubule structures reveal the structural transitions in αβ-tubulin upon GTP hydrolysis. *Cell* **157**, 1117–1129 (2014).
24. R. Zhang, B. LaFrance, E. Nogales, Separating the effects of nucleotide and EB binding on microtubule structure. *Proc. Natl. Acad. Sci. U.S.A.* **115**, E6191–E6200 (2018).
25. J. Estévez-Gallego *et al.*, Structural model for differential cap maturation at growing microtubule ends. *eLife* **9**, e50155 (2020).
26. J. LaFrance Benjamin *et al.*, Structural transitions in the GTP cap visualized by cryo-electron microscopy of catalytically inactive microtubules. *Proc. Natl. Acad. Sci. U.S.A.* **119**, e2114994119 (2022).
27. M. McCullagh, M. G. Saunders, G. A. Voth, Unraveling the mystery of ATP hydrolysis in actin filaments. *J. Am. Chem. Soc.* **136**, 13053–13058 (2014).
28. R. Sun, O. Sode, J. F. Dama, G. A. Voth, Simulating protein mediated hydrolysis of ATP and other nucleoside triphosphates by combining QM/MM molecular dynamics with advances in metadynamics. *J. Chem. Theory Comput.* **13**, 2332–2341 (2017).
29. I. Andricioaei, J. E. Straub, On Monte Carlo and molecular dynamics methods inspired by Tsallis statistics: Methodology, optimization, and application to atomic clusters. *J. Chem. Phys.* **107**, 9117–9124 (1997).
30. M. Salvalaglio, P. Tiwary, M. Parrinello, Assessing the reliability of the dynamics reconstructed from metadynamics. *J. Chem. Theory Comput.* **10**, 1420–1425 (2014).
31. S. Kumar, R. Nussinov, Close-range electrostatic interactions in proteins. *ChemBioChem* **3**, 604–617 (2002).
32. B. Musafia, V. Buchner, D. Arad, Complex salt bridges in proteins: Statistical analysis of structure and function. *J. Mol. Biol.* **254**, 761–770 (1995).
33. D. Tong, G. A. Voth, Microtubule simulations provide insight into the molecular mechanism underlying dynamic instability. *Biophys. J.* **118**, 2938–2951 (2020).
34. GROMACS 2019.4 Source Code (2019). https://doi.org/10.5281/zenodo.3460415.
35. J. Huang *et al.*, CHARMM36m: An improved force field for folded and intrinsically disordered proteins. *Nat. Methods* **14**, 71–73 (2017).
36. U. Essmann *et al.*, A smooth particle mesh Ewald method. *J. Chem. Phys.* **103**, 8577–8593 (1995).
37. T. D. Kühne *et al.*, CP2K: An electronic structure and molecular dynamics software package - Quickstep: Efficient and accurate electronic structure calculations. *J. Chem. Phys.* **152**, 194103 (2020).
38. T. Laino, F. Mohamed, A. Laio, M. Parrinello, An efficient real space multigrid QM/MM electrostatic coupling. *J. Chem. Theory Comput.* **1**, 1176–1184 (2005).
39. T. Laino, F. Mohamed, A. Laio, M. Parrinello, An efficient linear-scaling electrostatic coupling for treating periodic boundary conditions in QM/MM simulations. *J. Chem. Theory Comput.* **2**, 1370–1378 (2006).
40. J. VandeVondele *et al.*, Quickstep: Fast and accurate density functional calculations using a mixed Gaussian and plane waves approach. *Comput. Phys. Comm.* **167**, 103–128 (2005).
41. J. P. Perdew, K. Burke, M. Ernzerhof, Generalized gradient approximation made simple. *Phys. Rev. Lett.* **77**, 3865–3868 (1996).
42. S. Grimme, J. Antony, S. Ehrlich, H. Krieg, A consistent and accurate ab initio parametrization of density functional dispersion correction (DFT-D) for the 94 elements H-Pu. *J. Chem. Phys.* **132**, 154104 (2010).
43. S. Grimme, S. Ehrlich, L. Goerigk, Effect of the damping function in dispersion corrected density functional theory. *J. Comput. Chem.* **32**, 1456–1465 (2011).
44. N. Godbout, D. R. Salahub, J. Andzelm, E. Wimmer, Optimization of Gaussian-type basis sets for local spin density functional calculations. Part I Boron through neon, optimization technique and validation. *Can. J. Chem.* **70**, 560–571 (1992).
45. S. Goedecker, M. Teter, J. Hutter, Separable dual-space Gaussian pseudopotentials. *Phys. Rev. B* **54**, 1703–1710 (1996).
46. C. Hartwigsen, S. Goedecker, J. Hutter, Relativistic separable dual-space Gaussian pseudopotentials from H to Rn. *Phys. Rev. B* **58**, 3641–3662 (1998).
47. J. F. Dama, G. Rotskoff, M. Parrinello, G. A. Voth, Transition-tempered metadynamics: Robust, convergent metadynamics via on-the-fly transition barrier estimation. *J. Chem. Theory Computation* **10**, 3626–3633 (2014).
48. P. Raiteri, A. Laio, F. L. Gervasio, C. Micheletti, M. Parrinello, Efficient reconstruction of complex free energy landscapes by multiple walkers metadynamics. *J. Phys. Chem. B* **110**, 3533–3539 (2006).
49. G. A. Tribello, M. Bonomi, D. Branduardi, C. Camilloni, G. Bussi, PLUMED 2: New feathers for an old bird. *Comput. Phys. Commun.* **185**, 604–613 (2014).
50. M. Bonomi *et al.*, Promoting transparency and reproducibility in enhanced molecular simulations. *Nat. Methods* **16**, 670–673 (2019).
51. P. Hošek, V. Spiwok, Metadyn View: Fast web-based viewer of free energy surfaces calculated by metadynamics. *Comput. Phys. Commun.* **198**, 222–229 (2016).
52. G. Henkelman, H. Jónsson, Improved tangent estimate in the nudged elastic band method for finding minimum energy paths and saddle points. *J. Chem. Phys.* **113**, 9978–9985 (2000).